PNAS RESEARCH ARTICLE | ENGINEERING

Altermagnetic polar metallic phase in ultrathin epitaxially strained RuO_2 films

Seung Gyo Jeong[a,1,2], In Hyeok Choi[b,1,2], Sreejith Nair[a], Luca Buiarelli[a], Bita Pourbahari[c,d], Jin Young Oh[e], Bonnie Y.X. Lin[f], James M. LeBeau[f], Nabil Bassim[c,d], Daigorou Hirai[g], Ambrose Seo[h], Woo Seok Choi[e], Rafael M. Fernandes[i,j], Turan Birol[a], Liuyan Zhao[k], Jong Seok Lee[b,1], and Bharat Jalan[a,1]

Affiliations are included on p. 8.

Edited by Stuart Parkin, Max Planck Institute of Microstructure Physics, Halle (Saale), Germany; received September 20, 2025; accepted January 6, 2026

Altermagnetism refers to a wide class of magnetic orders featuring magnetic sublattices with opposite spins related by rotational symmetries, resulting in nontrivial spin splitting and magnetic multipoles. However, the direct observation of the altermagnetic transition remains elusive. Here, by combining theoretical analysis, electrical transport, X-ray, and optical spectroscopies, we establish a phase diagram in hybrid molecular beam epitaxy-grown RuO_2/TiO_2 (110) films, mapping symmetries along with altermagnetic/electronic/structural phase transitions as functions of film thickness and temperature. This features an altermagnetic metallic polar phase in epitaxially strained 2 nm films, suggesting a potential link between polar metals and altermagnetic materials. Such a clear signature of a magnetic phase transition at ~500 K is observed exclusively in ultrathin strained films, unlike in bulk RuO_2 single crystals. These results highlight the power of epitaxial heterostructure engineering to induce altermagnetism in systems initially nonmagnetic, opening avenues for realizing emergent quantum phases with multifunctional properties.

altermagnetism | RuO_2 thin film | strain | optical second harmonic generation | magneto-optics

Magnetic order, the self-organization of electron magnetic moments, breaks time-reversal symmetry often in conjunction with translational, inversion, and rotational symmetries (1–3). In noncompensated magnets like ferromagnets, Zeeman coupling causes nearly uniform splitting of the electronic energy bands between opposite spin states throughout the Brillouin zone. In contrast, conventional collinear antiferromagnets preserve spin-degeneracy in their band structures due to the combined time-reversal (TR) and translation or inversion symmetries. Recently, altermagnets have been identified as a new class of collinear compensated magnets where TR combined with rotation preserves the magnetic order (2, 4). They exhibit momentum-dependent spin-splitting with *d*-wave, *g*-wave, or *i*-wave symmetry, without a net magnetic moment (1–15). Recent experimental studies aimed at validating this novel phase have often relied on electrical transport and angle-resolved photoemission spectroscopy (ARPES) at low temperatures (16–23). However, direct probing of altermagnetic order parameters and coupled symmetries near the transition temperature remains challenging and thus missing.

Rutile RuO_2 has been one of the initial material candidates theoretically predicted to exhibit nonrelativistic spin-splitting (2, 16, 24). Experimentally, whether this compound displays any type of magnetism has become the center of ongoing debates. Bulk RuO_2 has the tetragonal $4/mmm$ ($P4_2/mnm$) structure and is expected to exhibit $4'/mmm'$ ($P4'_2/mnm'$) magnetic point (space) group hosting the antiferromagnetic order (1), where the magnetic moments point along the [001] axis. Earlier X-ray and neutron diffraction studies identified antiferromagnetic order with a small magnetic moment in bulk RuO_2 (25–27). However, recent muon spin rotation (μSR) spectroscopy and neutron diffraction experiments (28, 29), as well as optical conductivity and some ARPES studies (30, 31) have suggested a nonmagnetic phase of RuO_2 for bulk and/or strain-relaxed films (> 4 nm). This is consistent with density-functional-theory calculations with an added onsite repulsion (DFT+U), which reported that stoichiometric bulk RuO_2 does not have a magnetically ordered ground state unless the $+U$ added is unphysically large (24), although hole-doping or vacancies could lead to altermagnetism. Meanwhile, numerous experimental studies, particularly in RuO_2 films, have reported properties that are consistent with the presence of altermagnetism, possibly coexisting with some weak ferromagnetism, including spin-split bands (16, 32), magneto-optical (MO) effects (33), anomalous Hall effect (17, 32, 34), thermal spin transport (35, 36), and spin Hall effects (37–42). While it remains elusive to conclude whether RuO_2 is magnetic in general, experimental

Significance

Altermagnetism, a recently proposed form of magnetic order, has been predicted in rutile RuO_2 but its existence has remained controversial, as bulk crystals or thick films appear nonmagnetic. We demonstrate that epitaxial strain in ultrathin films stabilizes altermagnetism and enables direct observation of its magnetic transition using symmetry-sensitive magneto-optics, atomic-resolution probes, and theory. These results resolve long-standing debates about RuO_2 and reveal that strain can transform a nominally nonmagnetic material into an altermagnet. More broadly, our work establishes strain engineering as a powerful route to create emergent quantum states, advancing design strategies for functional oxides with potential applications in spintronics and quantum technologies.

Author contributions: S.G.J., I.H.C., J.S.L., and B.J. designed research; S.G.J., I.H.C., S.N., L.B., B.P., J.Y.O., B.Y.X.L., J.M.L., N.B., D.H., A.S., W.S.C., R.M.F., T.B., L.Z., J.S.L., and B.J. performed research; S.G.J., I.H.C., S.N., L.B., B.P., J.Y.O., B.Y.X.L., J.M.L., N.B., D.H., A.S., W.S.C., R.M.F., T.B., L.Z., J.S.L., and B.J. analyzed data; L.B., B.P., J.Y.O., B.Y.X.L., J.M.L., N.B., D.H., A.S., W.S.C., T.B., and L.Z. contributed to writing; and S.G.J., I.H.C., R.M.F., J.S.L., and B.J. wrote the paper.

The authors declare no competing interest.

This article is a PNAS Direct Submission.

[1]To whom correspondence may be addressed. Email: jeong397@umn.edu, jys2316@gm.gist.ac.kr, jsl@gist.ac.kr, or bjalan@umn.edu.

[2]S.G.J. and I.H.C. contributed equally to this work.

This article contains supporting information online at https://www.pnas.org/lookup/suppl/doi:10.1073/pnas.2526641123/-/DCSupplemental.

Published March 6, 2026.

observations suggest that RuO_2 films more commonly display magnetic behavior than bulk samples do. To shed light on this issue, it is essential to establish the role of epitaxial strain in influencing altermagnetism. This highlights the critical need for systematic investigations into magnetism and its associated magnetic transition behavior in high quality RuO_2 films as a function of strain. By modulating structural and electronic properties (43–45), strain can emerge as a key tuning parameter for the magnetic state of RuO_2.

To address this issue, we investigated strained RuO_2 films down to the nanometer thickness limit, using epitaxial RuO_2/TiO_2 (110) heterostructures grown by hybrid molecular beam epitaxy (hMBE). Crystal symmetry and magnetic order were characterized using symmetry-sensitive optical second harmonic generation (SHG) and MO effects (Fig. 1). By tracking the dependence of magnetic-SHG signal (46–49) and the MO signal (50, 51), we directly observe a change from a nonmagnetic point group to a magnetic point group below a transition temperature $T_c \sim 500$ K for fully strained films with thicknesses below 4 nm, consistent with an altermagnetic state. In contrast, no such signal was observed in bulk RuO_2 single crystals, which is in agreement with the previously reported nonmagnetic state in bulk RuO_2 sample from the μSR study (29). We attribute the unique magnetic behavior to the epitaxial strain present in ultrathin RuO_2 films, which is further supported by DFT calculations. Notably, we identified an altermagnetic polar metallic phase in epitaxially strained 2 nm RuO_2 film. Our findings offer novel insights into altermagnetism in rutile compounds and highlight the potential of epitaxial design for controlling altermagnets. Furthermore, this approach could be extended to a broader class of altermagnetic materials from initially nonmagnetic materials at bulk. Furthermore, the experimental observation of a polar metallic phase (52–55) coexisting with altermagnetism represents a previously unreported phase, underscoring the uniqueness and broader relevance of our work.

Results and Discussion

We first discuss the crystal structure of atomically flat RuO_2/TiO_2 (110) films as a function of film thickness (t) (*SI Appendix*, Fig. S1). Fig. 2*A* schematically illustrates the strained RuO_2/TiO_2 (110) film, with lattice mismatches of – 4.7% along [001] and + 2.3% along $[1\bar{1}0]$ (56, 57). This anisotropic strain reduces the crystalline symmetry of RuO_2 from tetragonal $P4_2/mnm$ to orthorhombic $Cmmm$, which can be further reduced to polar $Amm2$ due to interface effects in thin films (*SI Appendix*, Fig. S2). Fig. 2*B* shows that X-ray diffraction (XRD) reciprocal space maps (RSMs) at the (310) plane of 4 and 17 nm RuO_2 films demonstrating a fully strained state along $[1\bar{1}0]$ in the 4 nm film and partial relaxation in 17 nm film. Additionally, RSMs at the (332) plane (*SI Appendix*, Fig. S3) reveal the onset of strain relaxation along [001] for films with $t \geq 6$ nm. In contrast, although the diffraction signal from RuO_2 films thinner than 4 nm is too weak to resolve distinct peaks, the clear superlattice reflections observed in the 2 nm RuO_2/7 nm TiO_2 superlattice (*SI Appendix*, Fig. S3) confirm that the 2 nm RuO_2/TiO_2 layers remain fully strained along [001]. The high-angle annular dark-field scanning transmission electron microscopy (HAADF STEM) of an 11 nm RuO_2 film exhibits local dislocations along the [001] direction due to these strain relaxations (*SI Appendix*, Fig. S4), consistent with XRD results.

To investigate the symmetries of these films, we performed rotational anisotropy (RA) SHG measurements at an oblique angle θ in a reflection geometry by rotating the azimuthal angle φ relative to the in-plane crystal axis $[1\bar{1}0]$ (Fig. 1). The polarizations of fundamental and the SHG light were set to be parallel (P) or normal (S) to the incidence plane with P/S_{in}-P/S_{out} channels (equivalently PP, PS, SP, and SS). Fig. 2*C* shows the t-dependent evolution of SHG polar plots in the PP [$I^{PP}_{SHG}(\varphi)$, *Upper* panels] and SS configurations [$I^{SS}_{SHG}(\varphi)$, *Lower* panels] at $\theta = 45°$ and 560 K to focus on the crystalline symmetry characterization. The RA SHG patterns

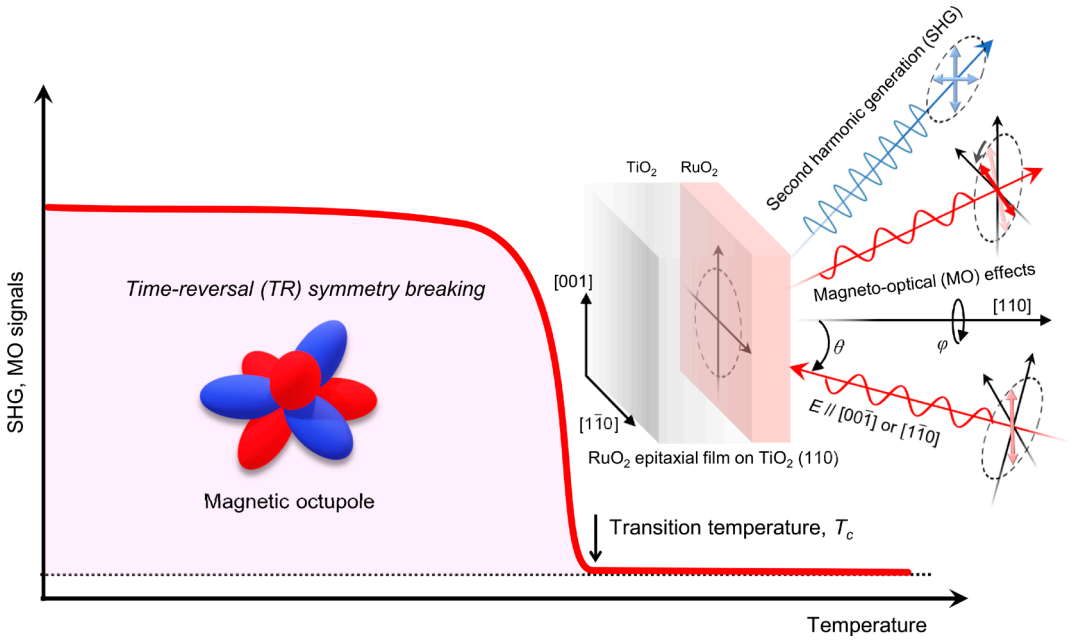

Fig. 1. Nonlinear- and magneto-optical signal revealing the altermagnetic transitions in RuO_2 epitaxial thin films. Schematic illustration of the SHG and MO signals leading to the observation of an altermagnetic transition that breaks TR symmetry below the transition temperature T_c. The inset shows a schematic description of the SHG and MO geometries. The SHG signal is proportional to the square of the nonlinear susceptibility ×. The altermagnetic order parameter, corresponding to the *d*-wave spin order, is illustrated by a magnetic octupole (see also DFT results in Fig. 4).

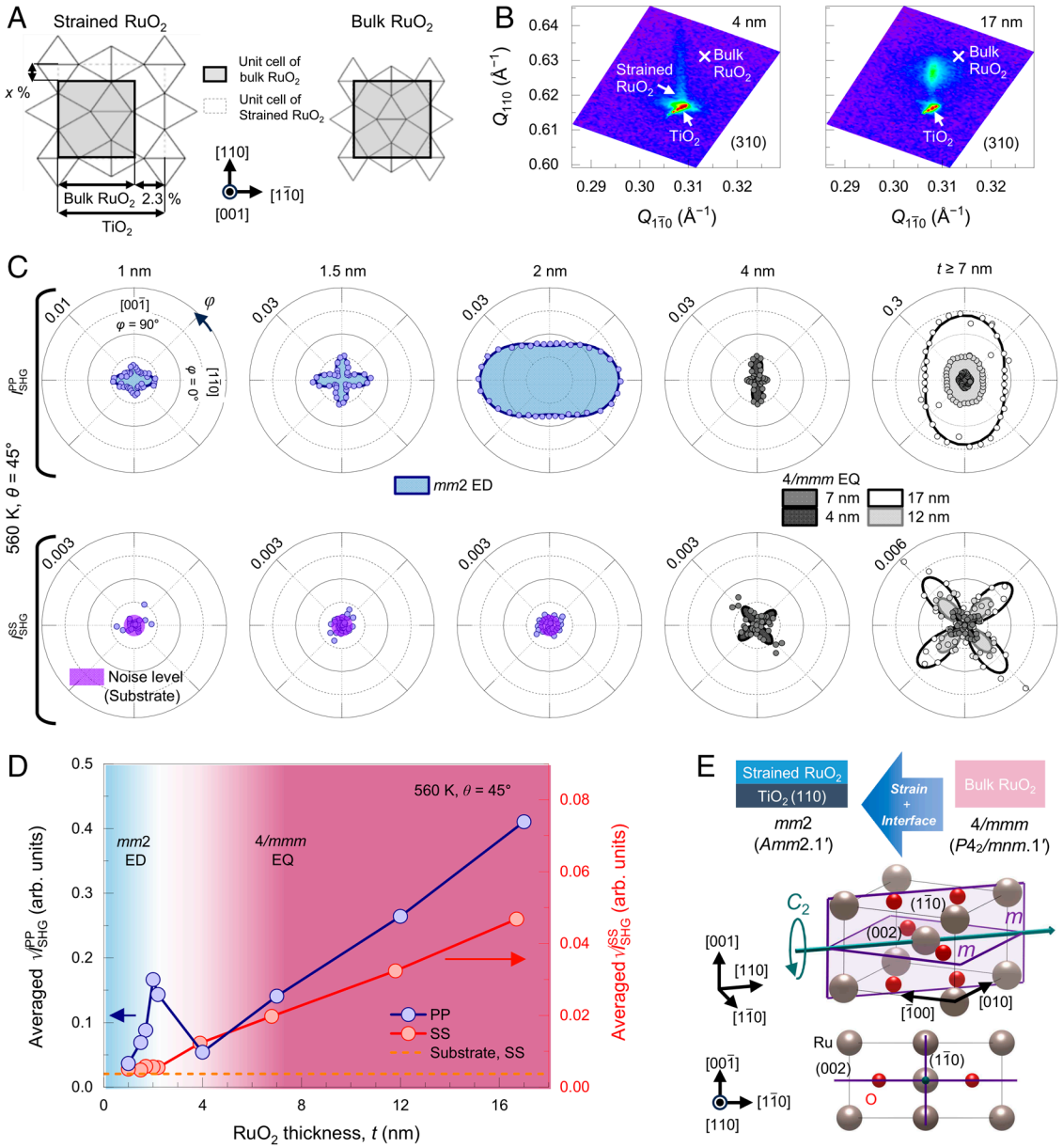

Fig. 2. Epitaxial strain-induced crystal symmetry evolution of RuO_2/TiO_2 (110) films. (*A*) Schematics of strain relations for RuO_2/TiO_2 (110) using bulk lattice values. *x* % is the lattice elongation along the [110] direction owing to the epitaxial strain. The gray square indicates the tetragonal unit cell of bulk 4/*mmm* RuO_2. (*B*), RSM XRD near (310) Bragg diffraction of TiO_2 for 4 and 17 nm RuO_2 films. (*C*) $I_{SHG}(\varphi)$ patterns with PP (*Upper* panels) and SS polarization (*Lower* panels) for RuO_2/TiO_2 (110) with different thickness *t*. The colored background and lines represent model fittings (details are in the main text). The noise level (purple) in I^{SS}_{SHG} estimated from the TiO_2 substrates. (*D*) *t*-dependent averaged $\sqrt{I_{SHG}}$ values for PP and SS polarizations at 560 K. The blue and red backgrounds represent regions where strained *mm*2 films (below 2 nm) and strain-relaxed 4/*mmm* (above 4 nm) are observed, respectively. (*E*) Conceptual illustration of structural phase transition from bulk RuO_2 to strained RuO_2/TiO_2 (110) thin films due to the combination of strain and interface effects. The *Bottom* panel schematically shows two mirror planes (*m*) and a twofold rotation axis (C_2) for the rutile *mm*2 structure.

showed pronounced *t*-dependence with abrupt changes for $t \geq 4$ nm. Fig. 2*D* presents the angular-averaged SHG field strengths as a function of *t*, i.e., $\sqrt{I^{\text{PP or SS}}_{\text{SHG}}(t)} = \sqrt{\sum_{\varphi} I^{\text{PP or SS}}_{\text{SHG}}(\varphi, t)}$, exhibits a *t*-dependent enhancement with distinct slopes for $t \leq 2$ nm and $t \geq 4$ nm, suggesting a structural phase transition as a function of *t*. Consistently, dramatic changes in crystal field energy observed from X-ray absorption spectroscopy (XAS) O *K*-edge (*SI Appendix*, Fig. S5 *A* and *B*), Hall coefficients (*SI Appendix*, Fig. S5*C*), and electronic structure modulations (58, 59) are also observed within the same thickness range.

Detailed analyses of the RA SHG patterns reveal the crystalline symmetries as a function of thickness. For strained RuO_2 films ($t \leq 2$ nm), I^{SS}_{SHG} is negligible, while the other polarization configurations exhibit twofold symmetric SHG responses. For example, in the $t = 2$ nm film (*SI Appendix*, Fig. S6), RA SHG in the PP, SP, and PS configurations exhibits a twofold rotational anisotropy about the [110] axis and two mirrors normal to the [1$\bar{1}$0] and [001] directions. These symmetries, revealing the breaking of the mirror perpendicular to the [110] axis, correspond to the noncentrosymmetric point group *mm*2, with the electric dipole contributions (ED, blue lines in Fig. 2*C*) dominating the SHG response for $t \leq 2$ nm (*SI Appendix*, Notes S1 and Table S1 and Figs. S6–S8). The θ-dependence of I_{SHG} further supports the *mm*2 symmetry for $t \leq 2$ nm (*SI Appendix*, Notes S2 and Fig. S9). Furthermore, for $t \leq 2$ nm, I_{SHG} increases with *t*, suggesting that ED SHG is a bulk response throughout the whole film thickness. Group theory shows that, starting from the tetragonal group

4/*mmm* of the bulk crystal, strain (or magnetic order) alone cannot induce the *mm*2 point group. Instead, a polar field along [110] is required, which can arise from interface effects or intrinsic polar symmetry breaking (*SI Appendix*, Fig. S2). Previous DFT calculations suggested that strain-induced zone-boundary lattice instabilities alone are insufficient (60), whereas an interface-induced polar field plays a critical role in establishing polarization throughout the RuO_2 film (Fig. 2*E*). We also confirmed the presence of interfacial polar displacements in $TiO_2/RuO_2/TiO_2$ heterostructures using STEM ptychography measurements (*SI Appendix*, Figs. S10 and S11). Meanwhile, in strain-relaxed films ($t \geq 4$ nm), the RA SHG patterns are well explained by the electric quadrupole (EQ) contribution to SHG with an underlying nonpolar, centrosymmetric point group 4/*mmm* (black and gray lines in Fig. 2*C*), consistent with bulk RuO_2. As t increases for $t \geq 4$ nm, both I_{SHG}^{PP} and I_{SHG}^{SS} increase, suggesting the bulk origin of 4/*mmm* EQ SHG.

The temperature dependence of the RA SHG shows clear evidence for time-reversal symmetry breaking in the strained RuO_2 films (i.e., films with $t \leq 4$ nm) below $T_c \sim 500$ K (Fig. 3 *A–C*). Fig. 3*A* compares $I_{SHG}^{PP}(\varphi)$ below T_c (320 and 420 K) and above T_c (540 K) for the 2 nm RuO_2 films. The anisotropy of $I_{SHG}^{PP}(\varphi)$ shows a significant temperature dependence with a large enhancement of the signal amplitude upon cooling, whereas I_{SHG}^{SS} shows no meaningful temperature dependence, remaining below the noise level (*SI Appendix*, Figs. S12 and S13). Most importantly, the symmetry of $I_{SHG}^{PP}(\varphi)$ below T_c is lower than its symmetry above T_c, signaling a phase transition. To verify whether there is a structural phase transition near T_c, we conducted temperature-dependent XRD and reflection high-energy electron diffraction (RHEED) measurements for the RuO_2 films (*SI Appendix*, Fig. S14). These measurements confirmed no structural transitions between 300 and 560 K. Thus, we attribute the temperature-dependent $I_{SHG}^{PP}(\varphi)$ to time-reversal

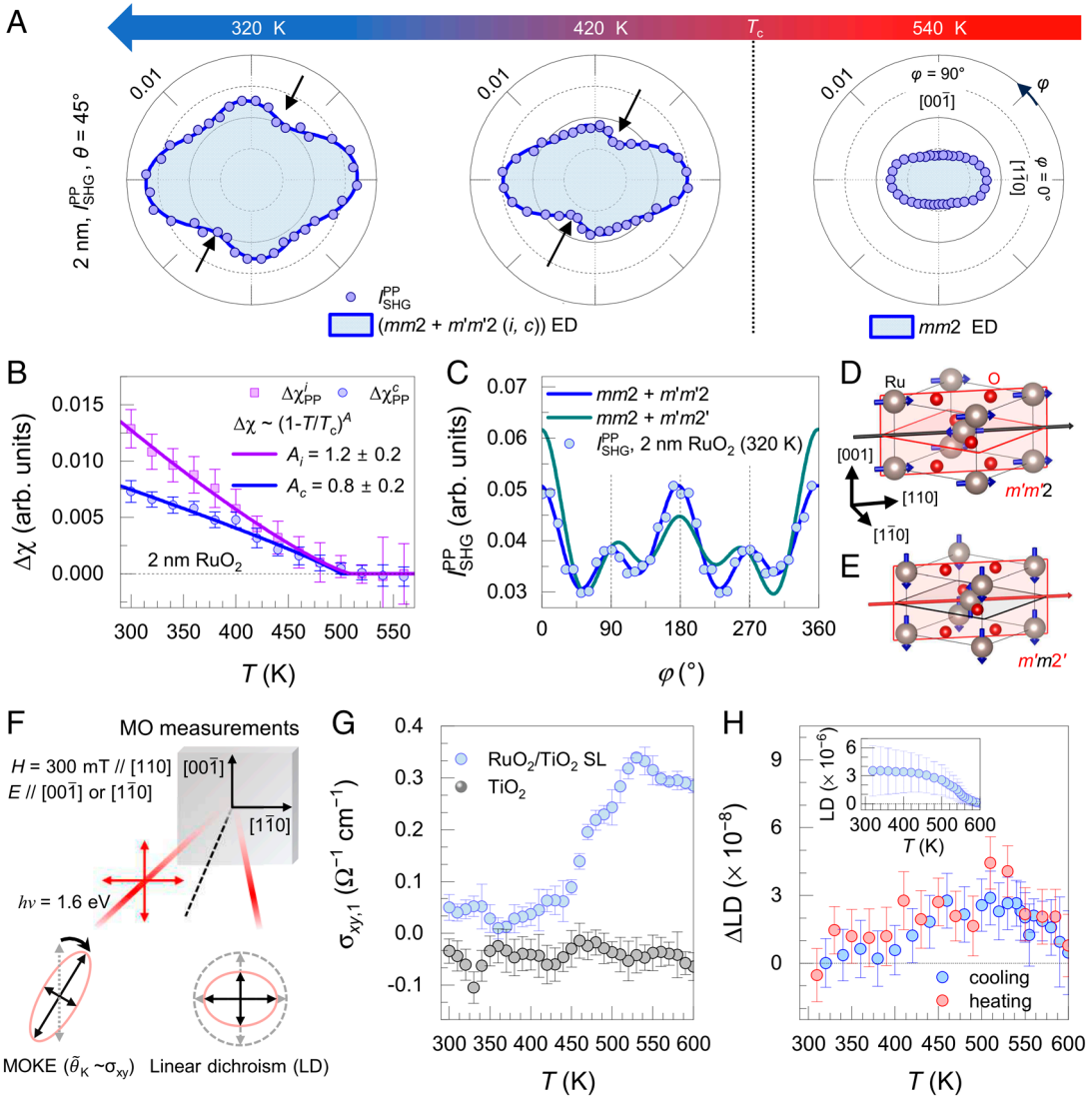

Fig. 3. Altermagnetic phase transition in strained RuO_2 heterostructures. (*A*) $I_{SHG}(\varphi)$ pattern evolution for the 2 nm film with PP polarization for 320, 420, and 540 K. The arrows denote the appearance of two dips at φ = 60° and 240° below T_c. (*B*) Temperature-dependent $\Delta\chi_{PP}^{i}$ and $\Delta\chi_{PP}^{c}$ for 2 nm. The solid lines are guides to the eye obtained from the phenomenological functional forms, $(1 - T/T_c)^A$, where T and A are the temperature and exponent parameters, respectively. A_i and A_c are exponent parameters for $\Delta\chi_{PP}^{i}$ and $\Delta\chi_{PP}^{c}$, respectively. (*C*) $I_{SHG}(\varphi)$ pattern for the 2 nm film at 320 K assuming two different symmetry groups. The vertical dashed line indicates the directions perpendicular to the mirrors. (*D* and *E*), Schematics of the mirror planes and twofold rotation axis in the magnetic point group resulting from magnetic moments oriented along (*D*) [110] (*m*′*m*′2) and (*E*) [001] (*m*′*m*2′, *Lower*) cases. The antichronous rotation and/or mirror elements are marked with a prime and red color. (*F*) MO experiments with 300 mT of out-of-plane *H*-field and 1.6 eV of excitation energy laser. (*G* and *H*) Temperature-dependent (*G*) $\sigma_{xy,1}$ and (*H*) ΔLD for the 2 nm RuO_2 SL. Here, *x* and *y* are [001] and [1$\bar{1}$0] directions, respectively. The inset of (*H*) shows a temperature-dependent static LD signal obtained from the ΔLD results during cooling. Error bars of $\sigma_{xy,1}$ and ΔLD were calculated from the SD of 50 data points.

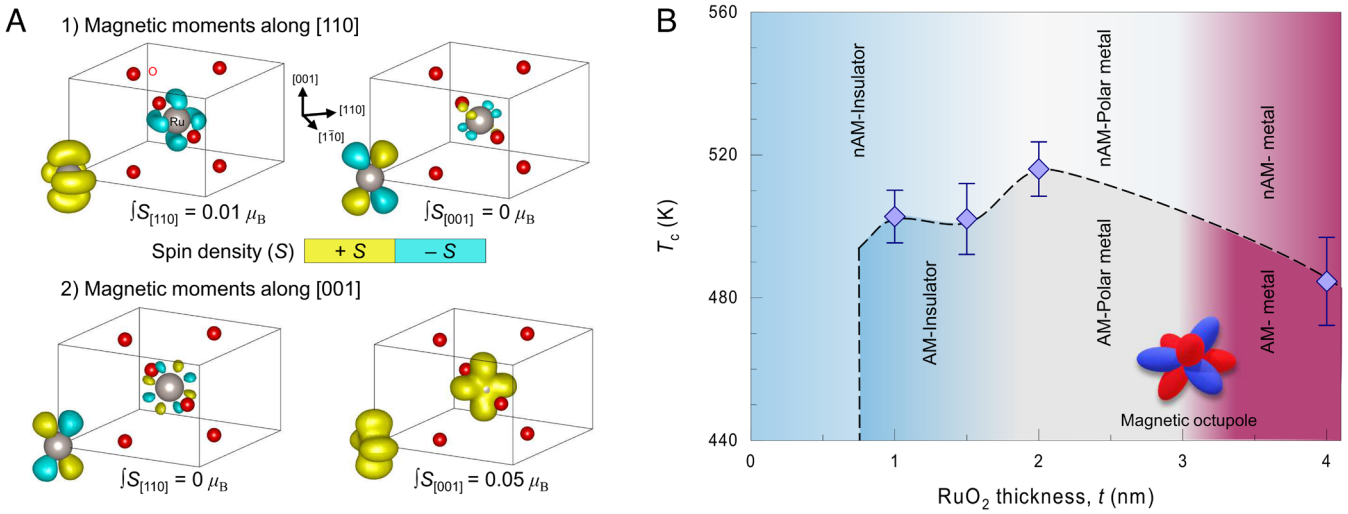

Fig. 4. Altermagnetic phase diagram of ultrathin RuO_2 films. (*A*) Calculated spin density of the [110] ($S_{[110]}$, *Left*) and [001] spin components ($S_{[001]}$, *Right*) for the cases of: 1) magnetic moments along [110] ($m'm'2$ magnetic point group) and 2) magnetic moments along [001] ($m'm2'$ magnetic point group). (*B*) Temperature-thickness phase diagram of ultrathin RuO_2 films. The blue symbols were obtained from the PP configurations of the SHG measurements. The inset illustrates schematically the magnetic octupole in altermagnetic RuO_2.

symmetry breaking in strained RuO_2 films. For the strain-relaxed 17 nm film, SHG data show no evidence of broken symmetry, remaining consistent with the tetragonal $4/mmm$ group across all temperatures (*SI Appendix*, Fig. S15). We also measured bulk RuO_2 single crystal, showing identical RA SHG patterns between 320 K and 520 K (*SI Appendix*, Fig. S16), consistent with μSR studies (29), highlighting the key role of epitaxial strain in the evolution of SHG signals in our 2 nm strained RuO_2 films.

To elucidate the origin of this broken symmetry, we plot in Fig. 3*B* the second-order susceptibility tensors $\Delta\chi^i_{PP}$ and $\Delta\chi^c_{PP}$ obtained from I^{PP}_{SHG}. Clearly, both $\Delta\chi^i_{PP}$ and $\Delta\chi^c_{PP}$ exhibit an anomaly around 500 K. Thus, the change in the symmetry of $I^{PP}_{SHG}(\varphi)$ can be attributed to nonlinear optical responses. As we explained above, at 540 K, $I^{PP}_{SHG}(\varphi)$ is mirror-symmetric for φ = 0° and 90° (dotted lines along [1$\bar{1}$0] and [001] in Fig. 3*C*), consistent with the structural point group $mm2$. However, at 320 K and 420 K, the twofold symmetric $I^{PP}_{SHG}(\varphi)$ shows dips at φ = 60° and 240° (marked by the arrows) that are absent at their mirror-symmetric angular counterparts φ = 120° and 300° (Figs. 3 *A* and *C*). This reveals that the strained 2 nm RuO_2 films break two mirrors normal to the [1$\bar{1}$0] and [001] directions, while retaining the twofold rotational axis along [110]. Since a structural transition was ruled out by our XRD and RHEED measurements, we consider whether a magnetic transition could lead to the broken mirrors observed experimentally. Starting with the paramagnetic group $mm2.1'$, we find that the magnetic subgroup with the highest symmetry has the same symmetries as $I^{PP}_{SHG}(\varphi)$ below T_c is $m'm'2$ (here, the prime indicates time-reversal symmetry). The key point is that the $m'm'2$ magnetic point group allows for both time-invariant (i-type) and time-variant (c-type) ED contributions to SHG, which scale with even and odd powers of the magnetic order parameter, respectively. The RA SHG at 320 K and 420 K fits well with the coherent interference between the i-type magnetic ED SHG of $m'm'2$ (or equivalently, structural ED SHG of $mm2$), contributing twofold and isotropic background signals, and c-type magnetic ED SHG of $m'm'2$, as shown by the blue line in Figs. 3 *A* and *C*. The identification of this magnetic group is also supported by the absence of I^{PP}_{SHG}.

Thus, we conclude that the strained RuO_2 thin films undergo a magnetic transition toward a ground state with magnetic point group $m'm'2$. This is the main result of our paper. Such a magnetic group naturally emerges by considering a translationally invariant compensated magnetic state with magnetic moments aligned along [110] (Fig. 3*D*). This is a primary altermagnetic state, since the magnetic moments in opposite sublattices are related by a nonsymmorphic symmetry (1–3), even though a secondary ferromagnetic order parameter is also allowed by symmetry. Note that this orientation of the moments is different from that theoretically proposed in bulk RuO_2 crystals (4, 17), where the moments point along [001] (Fig. 3*E*). In this case, the magnetic subgroup would be $m'm2'$, requiring mirror symmetry along [001] (*SI Appendix*, Notes S1). However, this contradicts our RA SHG data observations, which show no such mirror symmetry (green curve in Fig. 3*C*).

This $m'm'2$ altermagnetic state in the 2 nm-thick strained RuO_2 film is also confirmed by the MO measurements. Applying a magnetic-(H-) field along the [110] direction, the magneto-optical Kerr effect (MOKE) is symmetry-allowed for both $mm2$ and $m'm'2$, while the magnetic linear dichroism (LD) signal is only permitted for $m'm'2$ (*SI Appendix*, Table S2 and Notes S3). To enhance the MO signal in the ultrathin RuO_2 layer, we designed a superlattice consisting of alternating 2 nm RuO_2 and 1 nm TiO_2 layers with five repetitions, i.e., RuO_2/TiO_2 SL, showing a fully strained state in XRD (*SI Appendix*, Fig. S17) and similar optical spectrum with 2 nm RuO_2 single film (*SI Appendix*, Fig. S18). MOKE and magnetic LD measurements were conducted with alternating H-field (H = ± 300 mT) along the out-of-plane direction (Fig. 3*F*) to eliminate structural anisotropy contributions, and the results for strained RuO_2 showed distinct temperature-dependent behaviors (Figs. 3 *G* and *H* and *SI Appendix*, Fig. S19), consistent with symmetry predictions. In Fig. 3*G*, we observed a mild peak-like feature at 530 K in $\sigma_{xy,1}$ of the RuO_2/TiO_2 SL, obtained from complex Kerr angle $\tilde{\theta}_K$, whereas that of TiO_2 showed negligible values with no significant temperature-dependence. Since $\sigma_{xy,1}$ reflects the H-field-induced magnetic moment, proportional to magnetic susceptibility (61) (*SI Appendix*, Notes S4 and Fig. S20), this peak at T_c aligns with the expected Curie–Weiss law for an antiferromagnet, which peaks at the transition temperature. For the LD measurement, we pumped

the film with a pulsed laser and monitored the pump-induced changes in LD (ΔLD). Temperature-dependent ΔLD in Fig. 3*H* exhibits a broad peak-like feature at ~ 540 K, consistent with $\sigma_{xy,1}$. Since ΔLD is related to the thermo-LD coefficient (dLD/dT) and the pump-induced temperature increase (ΔT) as ΔLD ~ (dLD/dT) × ΔT, cumulative integration of ΔLD yields a signal directly proportional to the static LD. In the inset of Fig. 3*H*, the temperature-dependent LD signal increases starting around 540 K, indicating the development of an altermagnetic transition (*SI Appendix*, Fig. S21). These MO measurements thus provide direct evidence for a magnetic ground state in strained RuO_2 films, thereby validating our symmetry-based arguments.

To understand the altermagnetic state in strained RuO_2, we calculated the noncollinear spin density of RuO_2 for both $m'm'2$ and $m'm2'$ phases along the [110] and [001] spin components ($S_{[110]}$ and $S_{[001]}$) using DFT at $U = 0$ (Fig. 4*A*). Our calculations (*SI Appendix*, Tables S3–S6) show that epitaxial strain favors magnetism in a fully strained RuO_2 film even without U, and the addition of U only stabilizes the altermagnetic phase, in contrast to the nonmagnetic state of bulk RuO_2 at $U = 0$ (24), highlighting the distinct magnetic properties enabled by strain in RuO_2. While it is also possible to stabilize a phase with the same symmetry and parallel moments, the primary-altermagnetic state is lower in energy by ~1 meV per formula unit. The integrated spin density of the primary spin component (i.e., [110] for $m'm'2$ and [001] for $m'm2'$, respectively) yields a small, but nonzero integrated magnetic moment ($\int S \neq 0$), indicating that strained RuO_2 is no longer a compensated magnet. The secondary components, which are perpendicular to the magnetic moment orientation (i.e., [001] for $m'm'2$ and [110] for $m'm2'$, respectively), display the magnetic octupolar symmetry with a zero integrated magnetic moment ($\int S = 0$), further illustrating their altermagnetic nature. Therefore, the calculations suggest the coexistence of altermagnetism and weak-ferromagnetism in strained RuO_2 films.

To investigate the interplay between electrical properties and magnetism as t decreases, we performed temperature-dependent resistivity measurements. *SI Appendix*, Fig. S22 shows that RuO_2 films maintain metallic behavior down to t = 2 nm, whereas the 1.5 nm film transitions to an insulating state. The metallicity of the 2 nm RuO_2 film is further supported by the Drude response observed in optical spectroscopic ellipsometry (*SI Appendix*, Fig. S23). These results are summarized in a temperature-thickness phase diagram (Fig. 4*B*), highlighting the structural, electronic, and magnetic phases of RuO_2 films. Notably, an altermagnetic-$mm2$ (polar) metallic phase emerges at 2 nm, underscoring the versatility of RuO_2 epitaxial heterostructures. We also confirmed the presence of the magnetic-field-induced large nonlinear Hall effect in strained RuO_2 films, whereas no such effect was observed in strain-relaxed RuO_2 films (62). We examined the Ru valence state using X-ray photoelectron spectroscopy (XPS) and X-ray absorption spectroscopy (XAS) and consistently observed dominant Ru^{4+} oxidation states across all film thicknesses without any noticeable change in valence states (*SI Appendix*, Fig. S24).

The coexistence of various electronic and structural phases with magnetic transitions (above room temperature) down to 1 nm demonstrates the unique advantages of RuO_2 thin film for potential applications (*SI Appendix*, Table S7 for a summary of previous SHG studies). The absence of transition in 0.4 nm RuO_2 (*SI Appendix*, Figs. S12 and S13) likely reflects the dimensional limits of this magnetism.

In summary, our multiple experimental observations and theoretical analysis uncover the versatile electronic/magnetic/structural phases in epitaxial RuO_2 films. We reveal the fingerprints of the altermagnetic transition in strained RuO_2 film through nonlinear- and magneto-optical responses, which is not observed in RuO_2 bulk single crystal. Interestingly, a structural phase transition from the centrosymmetric $4/mmm$ to the inversion-symmetry-broken $mm2$ group is realized via heterostructure design, promoting an altermagnetic polar phase in strained RuO_2 film. Our study also points to a broader experimental strategy for detecting altermagnetic order through nonlinear and magneto-optical responses. By leveraging the symmetry sensitivity of nonlinear- and magneto-optical responses, we provide a pathway to probe altermagnetism in systems where conventional magnetometry has intrinsic difficulty, offering valuable tools for future explorations of this elusive magnetic state. The observed altermagnetic transitions open avenues for investigating unique phenomena and applications in the realm of oxide heterostructures and altermagnetic materials.

Materials and Methods

Solid-Source Metal-Organic hMBE. High-quality epitaxial RuO_2 films were synthesized using an oxide hMBE system (Scienta Omicron) on a TiO_2 (110) single crystalline substrate (Crystec). Solid-source metal-organic MBE has demonstrated high-quality RuO_2 thin films with an atomically flat surface, enabling precise and systematic analysis down to a nano-scale limit (*SI Appendix*, Fig. S1), which was never reported in any other film growth methods (63, 64). We utilized metal-organic precursor $Ru(acac)_3$, which was thermally evaporated using a low-temperature effusion cell (MBE Komponenten) set at an effusion cell temperature between 170 to 180 °C (56, 65). Before film growth, we performed a substrate treatment process with acetone, methanol, and isopropanol, followed by 2-h baking at 200 °C in a load lock chamber. We further performed a 20-min annealing in oxygen plasma at 300 °C of growth temperature before the film growth. We used radio frequency oxygen plasma operating at 250 W and an oxygen gas pressure of 5×10^{-6} Torr. After the growth, the sample was cooled to 120 °C in the presence of oxygen plasma to prevent the potential formation of oxygen vacancies. Our RuO_2 films were grown at 300 °C (thermocouple) and ~225 °C (actual temperature calibrated by pyrometer). Under such low-temperature conditions, the formation of Ru vacancies is highly suppressed. Moreover, the negative Hall coefficient of the 2 nm strained RuO_2 film (*SI Appendix*, Fig. S5*C*) indicates electron-type carriers, suggesting negligible hole doping associated with Ru vacancies.

Structure Characterization. High-resolution XRD measurements were performed using a Rigaku SmartLab XE and a PANalytical X'Pert XRD. We determined the crystallinity, film thickness, roughness, and strain state using reciprocal space mapping (RSM) and X-ray reflectivity and θ-2θ scans. For temperature-dependent XRD measurement, we used the sample heating stage of SmartLab XE with a spherical X-ray window (DHS-1100) in atmospheric conditions. We monitored film surfaces before, during, and after growth using in-situ reflection high-energy electron diffraction from Staib Instruments. Surface morphologies of RuO_2 films were further confirmed by using atomic force microscopy (Bruker Nanoscope V Multimode 8) with peakforce tapping mode.

Optical Second Harmonic Generation. SHG is a suitable observational tool for investigating both structural and magnetic symmetry and their correlation with magnetic orders. SHG has the unique advantage of probing magnetic transition by measuring temperature anomaly near T_c, summarized in *SI Appendix*, Table S7. We employed the SHG experiment in oblique incidence geometry with rotating the sample azimuth (φ) and incidence angle (θ). The fundamental beam (800 nm) is set to be P- or S-polarized, and we monitor the P- or S-polarized second harmonic beam. The notation PP and SS represent P_{in}–P_{out} and S_{in}–S_{out}, respectively. The incident beam is focused with a beam size of 30 μm and its power is about 50 mW. The SHG signal is measured using a photomultiplier detector (*Hamamatsu*), and we use both a short-pass and band-pass filter to eliminate the fundamental signal. We conducted all temperature-dependent SHG experiments in atmosphere conditions with the cooling process. To obtain the azimuth-dependent SHG polar pattern, we rotated the sample from 0° to 360°. For measuring the temperature-dependent SHG anisotropy pattern, we rotated the sample from 0° to 180°, and duplicated these results for the data from 180° to 360°. We have confirmed that duplicated data matches well the full-rotated data (*SI Appendix*, Fig. S25). The temperature dependence of $\Delta\chi^i_{PP}$ and $\Delta\chi^c_{PP}$

are obtained by subtracting their respective values at 560 K. The $\Delta\chi^{j}_{PP}$ and $\Delta\chi^{c}_{PP}$ corresponds to $\Delta(\chi_{zzz}+\chi_{zxx}+\chi_{zyy})$ and $\Delta(\chi_{xyz}+\chi_{xzy}+\chi_{yxz}+\chi_{yzx}-\chi_{zxy}-\chi_{zyx})$, respectively. We confirmed the consistent temperature dependence of SHG signal in the 2 nm RuO_2 film by sampling different positions and on different dates to ensure reproducibility (*SI Appendix*, Fig. S26).

Magneto-Optical Measurements. We conducted field-dependent magneto-optical Kerr effect (MOKE) and linear dichroism (LD) measurements on [2 nm RuO_2|1 nm TiO_2]$_5$ superlattices and the TiO_2 substrate to examine magnetic properties. All magneto-optic signals were obtained under an external magnetic field of 300 mT along the out-of-plane direction ([110]), and we extracted pure magnetic signals by alternatively changing the direction of the magnetic field. For MOKE measurements, complex Kerr angle ($\tilde{\theta}_K$) consisted of Kerr rotation angle (θ_K) and Kerr ellipticity (η_K) was obtained in a polar configuration, using an 80 MHz pulsed laser (Vision-S, *Coherent*). To selectively detect the signals from RuO_2 layers, we used 1.6 eV laser excitation below the TiO_2 band gap (~3 eV). In a polar configuration, the polarization of the laser was set along the [001] direction. To measure $\tilde{\theta}_K$, we modulated the probe beam with a photoelastic modulator (50 kHz), and the modulated signal was demodulated by a digital lock-in amplifier (*Zurich*), where the reference frequency is 50 kHz (1f) and 100 kHz (2f) for θ_K and η_K, respectively. The longitudinal conductivity ($\sigma_{xx,1}$) was obtained by ellipsometry at room temperature (*SI Appendix*, Fig. S18) and assumed to be temperature-independent. Through reflectance measurements with the 1.6 eV laser excitation, we observed a 4% decrease in the 560 K value compared to room temperature (*SI Appendix*, Fig. S27), which exhibits much smaller temperature dependence compared to the SHG and MOKE signals. Hence the room-temperature value of $\sigma_{xx,1}$ was taken for deducing the $\sigma_{xy,1}$ in Fig. 3*G*. A similar temperature dependence was observed in MOKE measurements using different positions and a laser excitation energy of 3.15 eV (*SI Appendix*, Fig. S28). For LD measurements, LD signals were obtained using a photoelastic modulator, alternatively modulating light polarizations between two orthogonal in-plane directions. We note that pump-induced changes in LD signal (ΔLD), rather than static LD signal, were measured to enhance the sensitivity to the optical anisotropy, as described in ref. 66. We confirmed the consistent temperature dependence of magnetic LD in the 2 nm RuO_2 superlattice by sampling different positions and on different dates to ensure reproducibility (*SI Appendix*, Fig. S29).

Electrical Transport Measurement. Temperature-dependent longitudinal and Hall resistances were measured in the van der Pauw geometry using the DynaCool Physical Property Measurement System (PPMS, Quantum Design). Ohmic contacts were obtained using aluminum wire bonding directly on the film.

Scanning Transmission Electron Microscopy. Scanning transmission electron microscopy (STEM) samples were prepared using a Focused Ion Beam Scanning Electron Microscope (FIB-SEM) equipped with a Ga ion gun (Thermo Fisher Helios 5 UC). Tungsten (W) and carbon (C) films were deposited on the area of interest before FIB milling to protect the surface from ion damage. A double-corrected HRTEM/STEM (TFS Spectra Ultra, operated at 300 keV) was used to acquire High Annular Angle Dark Field (HAADF) images of the RuO_2/TiO_2 interfaces, with sensitivity toward Ru and Ti lattices. The inverse FFT technique was used to unveil structural dislocation originating from strain relaxation during atomic-scale investigations.

Multislice Electron Ptychography. STEM samples for multislice electron ptychography were prepared using the conventional wedge polishing method. An aberration-corrected S/TEM (TFS Themis Z, operated at 300 kV) and an Electron Microscope Pixel Array Detector (EMPAD) (67) were used for collecting four-dimensional STEM (4D STEM) datasets. The diffraction pattern was sampled at 0.69 mrad/px for each scan position with a scan step size of 0.0,377 nm/px and a dwell time of 1 ms. The incident electron probe had a 26 mrad convergence semiangle, a 10 nm overfocus, and a beam current of 15 pA.

Ptychographic reconstructions were carried out through a modified version of the fold_slice (68) fork of the PtychoShelves (69) software package. The multislice reconstruction engine was a GPU-accelerated maximum-likelihood solver (70, 71). Partial coherence of the probe was incorporated by including 16 incoherent probe modes (72). The reconstruction involved four main steps, comprising a total of 760 iterations. The probe was not updated until after the initial 25 iterations in each step. The depth regularization parameter started at 1.0 and gradually reduced to 0.1 by the last step. By adding a few nanometers to the sample thickness estimated by the position averaged convergent beam electron diffraction (PACBED) patterns (73), the reconstruction thickness was maintained at 20 nm throughout all iterations, beginning at 4 layers and increasing to 20 layers in the final step, leading to a reconstruction result with twenty 1-nm-thick slices. By averaging only the middle three slices, the electron beam-induced structure and amorphous contamination on the surface were removed.

Density Functional Theory Calculation. Noncollinear DFT calculations with spin–orbit coupling were performed within the Local Density Approximation as implemented in ABINIT and using a basis of Projector Augmented Waves with Jollet-Torrent-Holzwarth PAW type pseudopotentials, using an energy cutoff of 550 eV (74–76). For all calculations, the Brillouin Zone (BZ) was sampled with a grid of 16 × 16 × 20 *k*-points centered at Γ. The bulk $P4_2/mnm$ structure was fully relaxed until the forces on each atom were less than 1 meV/Å. The strained (*Cmmm*) structure was obtained by fixing the strain on the directions $[1\bar{1}0]$ by + 2.5% and [001] by − 5% with respect to the relaxed bulk structure, and then allowing the components of the lattice parameters along the [110] direction and all ionic positions in the unit cell relax. The *Cm′m′m* (*Cmm′m′*) magnetic structure was obtained by imposing the initial spin-magnetization for the two Ru atoms as antiparallel along the [001] ([110]) direction in the strained structure *Cmmm*. The first principles calculations are limited to the centrosymmetric structures where the effects of magnetic order and strain are taken into account, but the interfacial dipolar field is ignored. The spinor wave functions ψ_{nk} of the electronic ground states were used to calculate the spin-magnetization in the real space unit cell,

$$S_i(\mathbf{r}) = \sum_{nk\ \text{occupied}} \psi^{\dagger}_{nk}(\mathbf{r})\sigma_i\psi_{nk}(\mathbf{r}),$$

where *n* indicates the band, *k* the *k*-point in the BZ and σ_i represent the three Pauli matrices with $i = x, y, z$. The three orthonormal Cartesian axes (*x, y, z*) are aligned with the orthogonal primitive lattice vectors (*a, b, c*) of the original, nonstrained, unit cell (in the strained case, *a* is kept aligned with *x*, while *b* acquires a small nonzero *x* component, but still lies in the *xy* plane). In Fig. 4*A*, $S_{[001]}$ is referred to as S_z, while $S_{[110]} = (S_x + S_y)/\sqrt{2}$. The isosurfaces were plotted using VESTA (77). For clarity, different isosurface values are used for each panel, and the ratio of the isosurface values for $S_{[110]}$ to $S_{[001]}$ is ~10 for the upper panels of Fig. 4*A*, and it is $\sim 10^{-1}$ for the lower panels. As enforced by the magnetic point groups, the integral of spin magnetic moment over the entire unit cell of $S_{[001]}$ in *Cmm′m′* (top-right) and $S_{[110]}$ in *Cm′m′m* (bottom-left) are zero. On the other hand, the integral of spin moment over the unit cell of $S_{[110]}$ in *Cmm′m′* (top-left) and $S_{[001]}$ in *Cm′m′m* are allowed to be nonzero, giving rise to the ferromagnetic moments in either the [110] or [001] directions. In the absence of strain, with symmetry $P4_2/mnm$, we find that the converged ground state without added +*U* has zero magnetic moments on the Ru ions, no matter the direction of the initial moments imposed. In the presence of strain, there is a notable difference. When we impose the moments to be antiparallel along the [001] direction, *Cm′m′m*, the converged ground state is weak-ferromagnetic (noncompensated altermagnetic) with a net moment of 0.05 μ_B along [001] in the unit cell. On the other hand, placing initial antiparallel moments along the direction [110], *Cmm′m′*, yields a weak-ferromagnetic with a net moment of 0.01 μ_B along [110]. Introduction of the +*U* correction favors the formation of local moments, and depending on the direction of the spins and the value of *U*, both parallel and antiparallel configurations of spins can be stabilized with a small energy difference, as discussed in *SI Appendix*, Tables S3–S6.

X-Ray Absorption Spectroscopy. X-ray absorption spectroscopy (XAS) measurements were performed at the 6A beamline of the Pohang Light Source in the total electron yield (TEY) mode for the O *K*-edge and Ru *L*-edge. XAS spectra were obtained at room temperature with surface normal configuration and σ polarization, where the electrical field direction of the X-rays is parallel to $[1\bar{1}0]$ crystal direction of RuO_2/TiO_2 (110) sample. We note that TEY is the surface-sensitive probing method, having the advantage of a surface state away from the substrate. Ru *L*-edge XAS spectra in *SI Appendix*, Fig. S24 show negligible energy shifts with similar bandwidths of the excitation peaks, indicating that the Ru ions predominantly maintain a +4 oxidation state.

X-Ray Photoelectron Spectroscopy. To confirm the chemical states of RuO_2 thin films, we measured core-level X-ray photoelectron spectroscopy (XPS, Physical Electronics VersaProbe III) for Ru 3*p* with a monochromatic Al Kα X-ray source (1,486.6 eV), as shown in *SI Appendix*, Fig. S24. We adopted a flood gun to compensate to prevent photoemission-induced surface charge effects. XPS spectrum was measured by an energy step size of 0.05 eV and a pass energy of 55 eV. We confirmed dominant Ru^{4+} oxidation states with no detectable evidence of other valence states for 2 and 7 nm films, consistent with XAS results.

Spectroscopic Ellipsometry. The optical conductivity spectrum was measured using spectroscopic ellipsometry (M-2000, J. A. Woollam Co., Inc.) at room temperature with photon energies ranging from 0.73 to 6.44 eV and incident angles of 60°, 65°, and 70°. The dielectric functions of the anisotropic RuO_2 (110) thin films along the $[1\bar{1}0]$ and [001] in-plane directions were extracted using a numerical iteration process with a biaxial anisotropic layer model. The dielectric functions of TiO_2 (110) were measured using a bare substrate. The consistency between the real and imaginary parts of the dielectric functions of RuO_2 thin films was checked with the Kramers–Kronig relations.

Data, Materials, and Software Availability. All data supporting the findings of this study are available in the main text and/or *SI Appendix*.

ACKNOWLEDGMENTS. The authors appreciate Zenji Hiroi for his assistance in the growth of RuO_2 single crystals conducted at the Institute for Solid State Physics, University of Tokyo. Structural characterization, transport, and ellipsometry at University of Minnesota (UMN) were supported by the Air Force Office of Scientific Research (AFOSR) through Grant No. FA9550-21-1-0025 and FA9550-24-1-0169. This work also benefitted from the Air Force Office of Scientific Research Multi University Research Initiative (AFOSR MURI, Award No. FA9550-25-1-0262). Film synthesis (S.G.J and B.J.) was supported by the U.S. Department of Energy through DE-SC0020211, and (partly) DE-SC0024710. S.N. was supported partially by the UMN Materials Research Science and Engineering Center (MRSEC) program under Award No. DMR-2011401. Parts of this work were carried out at the Characterization Facility at UMN which receives partial support from the NSF (NSF) through the MRSEC program under Award No. DMR-2011401. L.Z. acknowledges the support from Air Force Office of Scientific Research (AFOSR) Young Investigator Program (YIP) grant no. FA9550-21-1-0065 and NSF MRSEC DMR-2309029. Electron microscopy work was performed at the Canadian Centre for Electron Microscopy a core research facility at McMaster University (also supported by NSERC (Natural Sciences and Engineering Research Council of Canada) and the Canada Foundation for Innovation). B.P. and N.B. were supported by AFOSR Grant No. FA9550-23-1-0275 for electron microscopy research. A.S. acknowledges the support of NSF Grant No. DMR-2104296. R.M.F. was supported by the AFSOR under Award No. FA9550-21-1-0423. This work was supported by the National Research Foundation of Korea (NRF) grant funded by the Korea government (MSIT) [No. 2022R1A2C2007847 (I.H.C. and J.S.L.), 2022M3H4A1A04074153, 2021R1A2C2011340 (W.S.C.), and RS-2023-00220471 (W.S.C.)]. B.Y.X.L. and J.M.L. acknowledge support from the AFOSR through grant No. FA9550-20-1-0066. 4D-STEM dataset collection was carried out using the facilities at MIT.nano, and ptychographic reconstructions were enabled by MIT SuperCloud and Lincoln Laboratory Supercomputing Center. T.B. and L.B. were supported by the NSF through the University of Minnesota MRSEC under Award Number DMR-2011401.

Author affiliations: [a]Department of Chemical Engineering and Materials Science, University of Minnesota–Twin Cities, Minneapolis, MN 55455; [b]Department of Physics and Photon Science, Gwangju Institute of Science and Technology, Gwangju 61005, Republic of Korea; [c]Canadian Centre for Electron Microscopy and Department of Materials Science and Engineering, McMaster University, Hamilton, ON L8S 4L8, Canada; [d]Department of Materials Science and Engineering, McMaster University, Hamilton L8S 1L9, Canada; [e]Department of Physics, Sungkyunkwan University, Suwon 16419, Republic of Korea; [f]Department of Materials Science and Engineering, Massachusetts Institute of Technology, Cambridge, MA 02139; [g]Department of Applied Physics, Graduate School of Engineering, Nagoya University, Nagoya 464-8603, Japan; [h]Department of Physics and Astronomy, University of Kentucky, Lexington, KY 40506; [i]School of Physics and Astronomy, University of Minnesota–Twin Cities, Minneapolis, MN 55455; [j]Department of Physics, University of Illinois Urbana-Champaign, Urbana, IL 61801; and [k]Department of Physics, University of Michigan, Ann Arbor, MI 48109

1. L. Šmejkal, J. Sinova, T. Jungwirth, Emerging research landscape of altermagnetism. *Phys. Rev. X* **12**, 040501 (2022).
2. L. Šmejkal, J. Sinova, T. Jungwirth, Beyond conventional ferromagnetism and antiferromagnetism: A phase with nonrelativistic spin and crystal rotation symmetry. *Phys. Rev. X* **12**, 031042 (2022).
3. S. Hayami, Y. Yanagi, H. Kusunose, Momentum-dependent spin splitting by collinear antiferromagnetic ordering. *J. Phys. Soc. Japan* **88**, 123702 (2019).
4. L. Šmejkal, R. González-Hernández, T. Jungwirth, J. Sinova, Crystal time-reversal symmetry breaking and spontaneous Hall effect in collinear antiferromagnets. *Sci. Adv.* **6**, eaaz8809 (2020).
5. S. Bhowal, N. A. Spaldin, Ferroically ordered magnetic octupoles in d-wave altermagnets. *Phys. Rev. X* **14**, 011019 (2024).
6. R. M. Fernandes, V. S. Carvalho, T. Birol, R. G. Pereira, Topological transition from nodal to nodeless Zeeman splitting in altermagnets. *Phys. Rev. B* **109**, 024404 (2024).
7. K.-H. Ahn, A. Hariki, K.-W. Lee, J. Kuneš, Antiferromagnetism in RuO2 as d-wave Pomeranchuk instability. *Phys. Rev. B* **99**, 184432 (2019).
8. P. A. McClarty, J. G. Rau, Landau theory of altermagnetism. *Phys. Rev. Lett.* **132**, 176702 (2024).
9. S.-W. Cheong, F.-T. Huang, Altermagnetism with non-collinear spins. *NPJ Quantum Mater.* **9**, 13 (2024).
10. Y. Guo *et al.*, Spin-split collinear antiferromagnets: A large-scale ab-initio study. *Mater. Today Phys.* **32**, 100991 (2023).
11. I. Turek, Altermagnetism and magnetic groups with pseudoscalar electron spin. *Phys. Rev. B* **106**, 094432 (2022).
12. I. I. Mazin, K. Koepernik, M. D. Johannes, R. González-Hernández, L. Šmejkal, Prediction of unconventional magnetism in doped FeSb2. *Proc. Natl. Acad. Sci. U.S.A.* **118**, e2108924118 (2021).
13. I. I. Mazin, Altermagnetism in MnTe: Origin, predicted manifestations, and routes to detwinning. *Phys. Rev. B* **107**, L100418 (2023).
14. Y. Yu, T. Shishidou, S. Sumita, M. Weinert, D. F. Agterberg Spin-orbit enabled unconventional Stoner magnetism. *Proc. Natl. Acad. Sci. U.S.A.* **121**, e2411038121 (2024).
15. D. S. Antonenko, R. M. Fernandes, J. W. Venderbos, Mirror chern bands and weyl nodal loops in altermagnets. *Phys. Rev. Lett.* **134**, 096703 (2025).
16. O. Fedchenko *et al.*, Observation of time-reversal symmetry breaking in the band structure of altermagnetic RuO_2. *Sci. Adv.* **10**, eadj4883 (2024).
17. Z. Feng *et al.*, An anomalous hall effect in altermagnetic ruthenium dioxide. *Nat. Electron.* **5**, 735–743 (2022).
18. J. Krempaský *et al.*, Altermagnetic lifting of Kramers spin degeneracy. *Nature* **626**, 517–522 (2024).
19. R. D. Gonzalez Betancourt *et al.*, Spontaneous Anomalous Hall Effect Arising from an Unconventional Compensated Magnetic Phase in a Semiconductor. *Phys. Rev. Lett.* **130**, 036702 (2023).
20. S. Lee *et al.*, Broken Kramers degeneracy in altermagnetic MnTe. *Phys. Rev. Lett.* **132**, 036702 (2024).
21. T. Osumi *et al.*, Observation of a giant band splitting in altermagnetic MnTe. *Phys. Rev. B* **109**, 115102 (2024).
22. S. Reimers *et al.*, Direct observation of altermagnetic band splitting in CrSb thin films. *Nat. Commun.* **15**, 2116 (2024).
23. Z. Lin *et al.*, Observation of giant spin splitting and d-wave spin texture in room temperature altermagnet RuO_2. arXiv [Preprint] (2024), https://doi.org/10.48550/arXiv.2402.04995 (Accessed 7 February 2026).
24. A. Smolyanyuk, I. I. Mazin, L. Garcia-Gassull, R. Valentí, Fragility of the magnetic order in the prototypical altermagnet RuO_2. *Phys. Rev. B* **109**, 134424 (2024).
25. T. Berlijn *et al.*, Itinerant antiferromagnetism in RuO_2. *Phys. Rev. Lett.* **118**, 077201 (2017).
26. Z. H. Zhu *et al.*, Anomalous antiferromagnetism in metallic RuO_2 determined by resonant X-ray Scattering. *Phys. Rev. Lett.* **122**, 017202 (2019).
27. B. Z. Gregory *et al.*, Strain-induced orbital-energy shift in antiferromagnetic RuO_2 revealed by resonant elastic x-ray scattering. *Phys. Rev. B* **106**, 195135 (2022).
28. P. Keßler *et al.*, Absence of magnetic order in RuO_2: Insights from μSR spectroscopy and neutron diffraction. *NPJ Spintron.* **2**, 50 (2024).
29. M. Hiraishi *et al.*, Nonmagnetic ground state in RuO_2 revealed by muon spin rotation. *Phys. Rev. Lett.* **132**, 166702 (2024).
30. J. Liu *et al.*, Absence of altermagnetic spin splitting character in rutile oxide RuO_2. *Phys. Rev. Lett.* **133**, 176401 (2024).
31. M. Wenzel *et al.*, Fermi-liquid behavior of non-altermagnetic RuO_2. *Phys. Rev. B* **111**, L041115 (2025).
32. J. Song *et al.*, Spin-orbit coupling driven magnetic response in altermagnetic RuO_2. *Small.* **21**, e2407722 (2024).
33. M. Weber *et al.*, All optical excitation of spin polarization in d-wave altermagnets. arXiv [Preprint] (2024), https://doi.org/10.48550/arXiv.2408.05187 (Accessed 7 February 2026).
34. T. Tschirner *et al.*, Saturation of the anomalous Hall effect at high magnetic fields in altermagnetic RuO_2. *APL Mater.* **11**, 101103 (2023).
35. C.-T. Liao, Y.-C. Wang, Y.-C. Tien, S.-Y. Huang, D. Qu, Separation of inverse altermagnetic spin-splitting effect from inverse spin Hall effect in RuO_2. *Phys. Rev. Lett.* **133**, 056701 (2024).
36. H. Bai *et al.*, Efficient spin-to-charge conversion via altermagnetic spin splitting effect in antiferromagnet RuO_2. *Phys. Rev. Lett.* **130**, 216701 (2023).
37. S. Karube *et al.*, Observation of spin-splitter torque in collinear antiferromagnetic RuO_2. *Phys. Rev. Lett.* **129**, 137201 (2022).
38. H. Yan, X. Zhou, P. Qin, Z. Liu, Review on spin-split antiferromagnetic spintronics. *Appl. Phys. Lett.* **124**, 030503 (2024).
39. A. Bose *et al.*, Tilted spin current generated by the collinear antiferromagnet ruthenium dioxide. *Nat. Electron.* **5**, 267–274 (2022).
40. Y. Zhang *et al.*, Simultaneous high charge-spin conversion efficiency and large spin diffusion length in altermagnetic RuO_2. *Adv. Funct. Mater.* **34**, 2313332 (2024).
41. X. Feng *et al.*, Incommensurate spin density wave in antiferromagnetic RuO_2 evinced by abnormal spin splitting torque. *Phys. Rev. Lett.* **132**, 086701 (2024).
42. H. Bai *et al.*, Observation of spin splitting torque in a collinear antiferromagnet RuO2. *Phys. Rev. Lett.* **128**, 197202 (2022).
43. M. Fiebig, T. Lottermoser, D. Meier, M. Trassin, The evolution of multiferroics. *Nat. Rev. Mater.* **1**, 16046 (2016).

44. J. H. Haeni *et al.*, Room-temperature ferroelectricity in strained $SrTiO_3$. *Nature* **430**, 758–761 (2004).
45. S. G. Jeong, J. Y. Oh, L. Hao, J. Liu, W. S. Choi, Correlated quantum phenomena of spin-orbit coupled perovskite oxide heterostructures: Cases of $SrRuO_3$ and $SrIrO_3$ based artificial superlattices. *Adv. Funct. Mater.* **33**, 2301770 (2023).
46. L. Zhao *et al.*, Evidence of an odd-parity hidden order in a spin–orbit coupled correlated iridate. *Nat. Phys.* **12**, 32–36 (2016).
47. L. Zhao *et al.*, A global inversion-symmetry-broken phase inside the pseudogap region of $YBa_2Cu_3O_y$. *Nat. Phys.* **13**, 250–254 (2017).
48. Y. Ahn *et al.*, Electric quadrupole second-harmonic generation revealing dual magnetic orders in a magnetic Weyl semimetal. *Nat. Photonics* **18**, 26–31 (2024).
49. M. Fiebig, V. V. Pavlov, R. V. Pisarev, Second-harmonic generation as a tool for studying electronic and magnetic structures of crystals: Review. *J. Opt. Soc. Am. B Opt. Phys.* **22**, 96–118 (2005).
50. C. S. Arnold, M. Dunlavy, D. Venus, Magnetic susceptibility measurements of ultrathin films using the surface magneto-optic Kerr effect: Optimization of the signal-to-noise ratio. *Rev. Sci. Instrum.* **68**, 4212–4216 (1997).
51. A. Aspelmeier *et al.*, Ac susceptibility measurements of magnetic monolayers: MCXD, MOKE, and mutual inductance. *J. Magn. Magn. Mater.* **146**, 256–266 (1995).
52. S. Bhowal, N. A. Spaldin, Polar metals: Principles and prospects. *Annu. Rev. Mater. Res.* **53**, 53–79 (2023).
53. Y. Shi *et al.*, A ferroelectric-like structural transition in a metal. *Nat. Mater.* **12**, 1024–1027 (2013).
54. T. H. Kim *et al.*, Polar metals by geometric design. *Nature* **533**, 68–72 (2016).
55. D. Hickox-Young, D. Puggioni, J. M. Rondinelli, Polar metals taxonomy for materials classification and discovery. *Phys. Rev. Mater.* **7**, 010301 (2023).
56. W. Nunn *et al.*, Solid-source metal–organic molecular beam epitaxy of epitaxial RuO_2. *APL Mater.* **9**, 091112 (2021).
57. J. P. Ruf *et al.*, Strain-stabilized superconductivity. *Nat. Commun.* **12**, 59 (2021).
58. S. G. Jeong *et al.* Anisotropic strain relaxation-induced directional ultrafast carrier dynamics in RuO2 films. *Sci. Adv.* **11**, eadw7125 (2025).
59. Y. Zhang *et al.*, Observation of mirror-odd and mirror-even spin texture in ultra-thin epitaxially-strained RuO_2 films. arXiv [Preprint] (2025), https://doi.org/10.48550/arXiv.2509.16361 (Accessed 7 February 2026).
60. M. Uchida, T. Nomoto, M. Musashi, R. Arita, M. Kawasaki, Superconductivity in uniquely strained RuO_2 films. *Phys. Rev. Lett.* **125**, 147001 (2020).
61. V. V. Eremenko, N. F. Kharchenko, Magneto-optics of antiferromagnets. *Phys. Rep.* **155**, 379–401 (1987).
62. S. G. Jeong *et al.* Metallicity and anomalous Hall effect in epitaxially strained, atomically thin RuO_2 films. *Proc. Natl. Acad. Sci. U.S.A.***122**, e2500831122 (2025).
63. S. S. Fields, P. G. Callahan, N. G. Combs, C. D. Cress, S. P. Bennett, Orientation control and mosaicity in heteroepitaxial RuO_2 thin films grown through reactive direct current sputtering. *Cryst. Growth Des.* **24**, 4604–4612 (2024).
64. P. Keßler *et al.*, Epitaxial RuO2 and IrO2 films by pulsed laser deposition on TiO_2(110). *APL Mater.* **12**, 101110. (2024).
65. S. Nair *et al.*, Engineering metal oxidation using epitaxial strain. *Nat. Nanotechnol.* **18**, 1005–1011 (2023).
66. V. Saidl *et al.*, Optical determination of the Néel vector in a CuMnAs thin-film antiferromagnet. *Nat. Photonics* **11**, 91–96 (2017).
67. M. W. Tate *et al.*, High dynamic range pixel array detector for scanning transmission electron microscopy. *Microsc. Microanal.* **22**, 237–249 (2016).
68. Z. Chen *et al.*, Electron ptychography achieves atomic-resolution limits set by lattice vibrations. *Science* **372**, 826–831 (2021).
69. K. Wakonig *et al.*, PtychoShelves, a versatile high-level framework for high-performance analysis of ptychographic data. *J. Appl. Crystallogr.* **53**, 574–586 (2020).
70. P. Thibault, M. Guizar-Sicairos, Maximum-likelihood refinement for coherent diffractive imaging. *New J. Phys.* **14**, 063004 (2012).
71. P. Thibault, A. Menzel, Reconstructing state mixtures from diffraction measurements. *Nature* **494**, 68–71 (2013).
72. E. H. R. Tsai, I. Usov, A. Diaz, A. Menzel, M. Guizar-Sicairos, X-ray ptychography with extended depth of field. *Opt. Express* **24**, 29089–29108 (2016).
73. J. M. LeBeau, S. D. Findlay, L. J. Allen, S. Stemmer, Position averaged convergent beam electron diffraction: Theory and applications. *Ultramicroscopy* **110**, 118–125 (2010).
74. X. Gonze *et al.*, The Abinitproject: Impact, environment and recent developments. *Comput. Phys. Commun.* **248**, 107042 (2020).
75. A. H. Romero *et al.*, ABINIT: Overview and focus on selected capabilities. *J. Chem. Phys.* **152**, 124102 (2020).
76. M. Torrent, F. Jollet, F. Bottin, G. Zérah, X. Gonze, Implementation of the projector augmented-wave method in the ABINIT code: Application to the study of iron under pressure. *Comput. Mater. Sci.* **42**, 337–351 (2008).
77. K. Momma, F. Izumi, VESTA 3 for three-dimensional visualization of crystal, volumetric and morphology data. *J. Appl. Crystallogr.* **44**, 1272–1276 (2011).